Journal of Materials Chemistry C

PAPER

View Article Online
View Journal | View Issue

Cite this: J. Mater. Chem. C, 2019, 7, 10851

High-efficiency pure blue thermally activated delayed fluorescence emitters with a preferentially horizontal emitting dipole orientation *via* a spiro-linked double D–A molecular architecture†

Xuan Zeng,[ab] Kuan-Chung Pan,[c] Wei-Kai Lee,[c] Shaolong Gong,*[a] Fan Ni,[b] Xiao Xiao,[a] Weixuan Zeng,[a] Yepeng Xiang,[a] Lisi Zhan,[a] Yu Zhang,[a] Chung-Chih Wu*[c] and Chuluo Yang*[ab]

Blue as one of the three primary colors is of great significance for lighting and full-color displays, and the development of blue emitters with satisfactory color purity and high efficiency is still a formidable challenge for organic light-emitting diodes (OLEDs). In this study, a spiro-linked double donor–acceptor (D–A) molecular architecture is introduced to selectively improve the horizontal emitting dipole orientation of blue emitters and thereby boost the electroluminescence (EL) performance of blue OLEDs. To testify the validity, a thermally activated delayed fluorescence (TADF) emitter, namely **SBA-2DPS**, is designed by connecting two D–A pairs with a sp^3 hybrid carbon atom. Compared to the prototypical emitter **DMAC-1DPS**, the shape of **SBA-2DPS** is elongated dramatically without expanding the degree of π-conjugation owing to the σ-spacer linkage. Consequently, a high horizontal dipole ratio ($\Theta_{\parallel}$ = 87%) is achieved for **SBA-2DPS**. Besides, **SBA-2DPS** exhibits high thermal stability, pure blue emission and distinct TADF characteristics. OLEDs based on **SBA-2DPS** exhibit an external quantum efficiency (η_{ext}) of 25.5% and favorable Commission International de l'Eclairage (CIE) coordinates of (0.15, 0.20). Such an inspiring performance is rationalized by their high out-coupling efficiency (Φ_{out} = 38.2%) and the optical microcavity effect. Unambiguously, this finding demonstrates the validity of the spiro-linked double D–A molecular architecture in constructing good blue TADF emitters with a preferentially horizontal emitting dipole orientation for high-efficiency blue OLEDs.

Received 3rd July 2019,
Accepted 1st August 2019

DOI: 10.1039/c9tc03582f

rsc.li/materials-c

Introduction

Organic light-emitting diodes (OLEDs) have been regarded as a promising light source for flat-panel displays and solid-state lighting owing to their various advantages, such as being flexible and lightweight and having low-power-consuming characteristics.[1–3] Since first reported by Tang and Van Slyke, the common goal for OLEDs is to boost their electroluminescence (EL) performance, especially external quantum efficiencies (η_{ext}s).[4–7] As an important factor to characterize the EL efficiencies of OLEDs, η_{ext} is determined using the following factors:[8]

$$\eta_{ext} = \gamma\eta_r\Phi_{PL}\Phi_{out} \quad (1)$$

where γ is the charge balance factor, which can be close to unity by device optimization; η_r is the fraction of radiative excitons determined by spin statistics; Φ_{PL} refers to the photoluminescence quantum yield (PLQY) and can also approach 100% with a suitable molecular design; Φ_{out} represents the optical out-coupling efficiency, which is normally less than 25% for conventional planar OLEDs with isotropically oriented emitters.[9] With respect to conventional fluorescent emitters, only 25% of singlet excitons can be harvested by radiative processes, leading

[a] Hubei Key Lab on Organic and Polymeric Optoelectronic Materials, Department of Chemistry, and Renmin Hospital of Wuhan University, Wuhan University, Wuhan, 430072, People's Republic of China. E-mail: slgong@whu.edu.cn, clyang@whu.edu.cn
[b] College of Materials Science and Engineering, Shenzhen University, Shenzhen 518060, People's Republic of China
[c] Department of Electrical Engineering, Graduate Institute of Electronics Engineering and Graduate, Institute of Photonics and Optoelectronics, National Taiwan University, Taipei 10617, Taiwan. E-mail: wucc@ntu.edu.tw

† Electronic supplementary information (ESI) available: Material synthesis, X-ray structural analysis, photophysical characterization, device fabrication and measurements, DSC curves, analysis of rate constants, and ^{1}H and ^{13}C NMR spectra. CCDC 1868667 and 1868668. For ESI and crystallographic data in CIF or other electronic format see DOI: 10.1039/c9tc03582f

to poor device performance with an upper limit η_{ext} of 5%.[10,11] To address this issue, many efforts have been devoted to exploring novel emitters with a higher η_r by harnessing 75% of triplet excitons.[12–14] Among them, the most successful one is phosphorescent heavy-metal complexes that could harness both singlet and triplet excitons by spin–orbital coupling.[15,16] However, the introduction of noble metals such as iridium (Ir) and platinum (Pt) raises the material cost and thus restricts their commercial applications.[17] In this context, thermally activated delayed fluorescence (TADF) emitters have emerged as a promising alternative due to their ability to harvest triplet excitons by a reverse intersystem crossing (RISC) process without involving noble metals.[6,18–20] Apart from η_r, another key factor in determining η_{ext} is Φ_{out} according to eqn (1). As mentioned above, the value of Φ_{out} is usually less than 25% for conventional planar OLEDs with isotropically oriented emitters. However, this value can be upgraded to over 45% for emitters with a perfectly horizontal emitting dipole orientation even in the absence of optical out-coupling structures, mainly due to the reduction of surface plasmon coupling at the organic/cathode interface and more favorable radiation patterns of horizontal dipoles for direct optical out-coupling.[21] Therefore, enhancing the horizontal dipole ratios of emitters has become an effective approach for achieving high Φ_{out}s in OLEDs.

Taking η_r and Φ_{out} into account, developing TADF emitters with a preferentially horizontal emitting dipole orientation will further boost their EL performance.[20,22–24] Some strategies have been proposed to increase the horizontal dipole ratios of TADF emitters.[25] In some cases, when a transition dipole moment (TDM) locates along the long axis of a molecule or in the molecular plane, the horizontal dipole ratio can be promoted by altering the molecular shapes, such as elongating the molecular length or broadening the molecular planarity.[26] However, these strategies may enlarge the degree of π-conjugation of TADF molecules and cause a redshift in their emission spectra, making them unsuitable for designing blue TADF emitters, especially in the pure blue or deep blue region.[27] Therefore, a judicious strategy is highly desirable for modulating the molecular shapes of blue TADF emitters to achieve high horizontal dipole ratios while maintaining their limited molecular conjugation.

In this study, a spiro-linked double D–A molecular architecture was introduced to construct rod-like TADF emitters, which will selectively elongate the molecular shape, but barely affect the degree of π-conjugation owing to the σ-spacer linkage between two counterparts. As shown in Fig. 1a, a TADF emitter, namely **SBA-2DPS**, possessing diphenyl sulfone (DPS) as an electron acceptor (A) unit and spirobiacridine (SBA) as an electron donor (D) unit was designed and synthesized. For comparison, a prototypical molecule **DMAC-1DPS** was also synthesized and had a single counterpart possessing the DPS acceptor and a 9,9-dimethyl-9,10-dihydroacridine (DMAC) donor. Further studies using molecular simulations and experiments demonstrated that the molecular length of **SBA-2DPS** was significantly elongated without extending the π-conjugation compared to **DMAC-1DPS**. As a result, **SBA-2DPS** showed blue emission with a moderate Φ_{PL} value and distinct TADF properties like

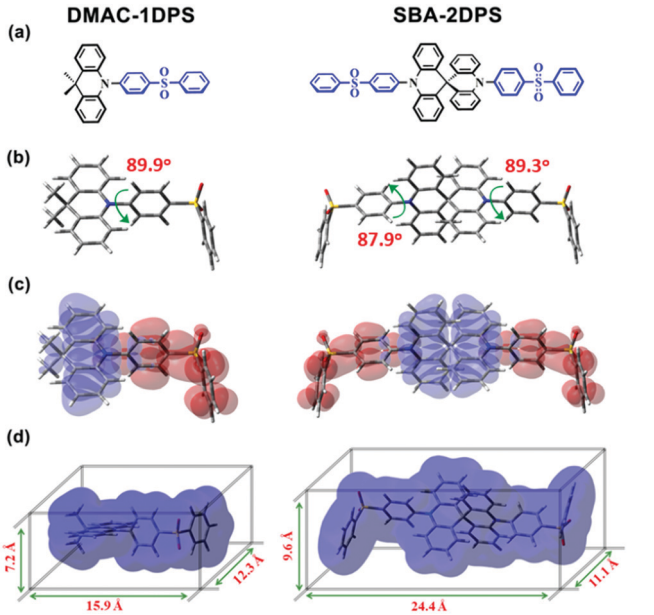

Fig. 1 (a) Molecular structures, (b) optimized ground state structures, (c) the HOMO (blue) and LUMO (red) distributions with optimized ground state structures, (d) isodensity surface of the designed molecules with ρ = 0.001 e Bohr^{-3}.

DMAC-1DPS, but exhibited a much higher horizontal dipole ratio $\Theta_{\parallel}$ of 87% in comparison with 59% for **DMAC-1DPS**. Consequently, OLEDs employing **SBA-2DPS** as an emitter showed pure blue emission with Commission International de l'Eclairage (CIE) coordinates of (0.15, 0.20), and exhibited excellent EL performance with a peak η_{ext} of 25.5%. This performance is outstanding compared with that of the best blue TADF emitters with similar color coordinates.[28,29] These results testify the validity of the spiro-linked double D–A molecular architecture in developing pure blue TADF emitters with high $\Theta_{\parallel}$ and η_{ext}.

Results and discussion

DFT calculations

It is known that the well-separated frontier molecular orbitals (FMOs) can result in a small energy gap (ΔE_{ST}) between the lowest excited singlet (S_1) and triplet (T_1) states.[30,31] Therefore, density functional theory (DFT) calculations were performed to predict the FMOs and electronic properties of the designed molecules at first. As shown in Fig. 1b, both molecules showed a highly twisted structure in the ground state with dihedral angles, between the DMAC or SBA moiety and the DPS unit, of 89.9° for **DMAC-1DPS**, and 87.9°/89.3° for **SBA-2DPS**. Accordingly, the highest occupied molecular orbitals (HOMOs) of both emitters were mainly located on the DMAC or SBA moieties, while their lowest unoccupied molecular orbitals (LUMOs) were mainly localized on the DPS moiety, exhibiting a small overlap between the HOMOs and LUMOs (Fig. 1c). Furthermore, time-dependent DFT (TD-DFT) calculations based on the optimized ground structure were conducted to study their excited states. As summarized in Table 1, the energy levels of S_1/T_1 were estimated to be 3.42/3.27 eV

Table 1 Key data obtained from the DFT and TD-DFT calculations

Compound	HOMO[a] [eV]	LUMO[a] [eV]	Energy level[b] [eV]			X_{max}/X_{min}[c] [Å]	Y_{max}/Y_{min}[c] [Å]	Z_{max}/Z_{min}[c] [Å]
			S_1	T_1	ΔE_{ST}			
DMAC-1DPS	−5.07	−1.58	3.42	3.27	0.15	8.1/−7.8	6.4/−5.9	3.6/−3.6
SBA-2DPS	−5.17	−1.63	3.31	3.23	0.08	12.2/−12.2	5.4/−5.7	4.8/−4.8

[a] Obtained from DFT calculations. [b] Obtained from TD-DFT calculations with the optimized ground state structure. [c] The spatial range of the emitter's isodensity surface in the Cartesian axes generated by the Marching Tetrahedra (MT) approach. X_{max}/X_{min}, Y_{max}/Y_{min} and Z_{max}/Z_{min} are the maximum/minimum values of the isodensity surface in the x axis, y axis and z axis, respectively.

for **DMAC-1DPS** and 3.31/3.23 eV for **SBA-2DPS**. In comparison with **DMAC-1DPS**, the π-conjugation of **SBA-2DPS** is barely affected owing to the σ-spacer linkage of the sp^3 hybrid carbon atom. Correspondingly, the ΔE_{ST} values for both molecules were calculated to be 0.15 eV for **DMAC-1DPS** and 0.08 eV for **SBA-2DPS**, suggesting that the designed molecules could be potential TADF materials.[32] Moreover, considering the correlation between molecular orientation and molecular shape, the spatial ranges of both molecules were quantified using the isodensity surface at ρ = 0.001 e $Bohr^{-3}$ generated by the Marching Tetrahedra (MT) approach with their optimized ground state structures (Fig. 1d and Table 1).[33] Along the x axis in molecular cartesian coordinates, X_{max} and X_{min} were estimated to be 12.2 Å and −12.2 Å for **SBA-2DPS**, and 8.1 Å and −7.8 Å for **DMAC-1DPS**, respectively. Apparently, the molecular length of **SBA-2DPS** along its long axis is 1.53 fold longer than that of **DMAC-1DPS**. Meanwhile, the aspect ratios of length to width for both molecules were also determined to be 2.20 for **SBA-2DPS** and 1.29 for **DMAC-1DPS**. These results manifest that **SBA-2DPS** possesses a more linear shape than **DMAC-1DPS**, which indicates that **SBA-2DPS** has a better horizontal molecular orientation.[34]

Synthesis and characterization

DMAC-1DPS and **SBA-2DPS** were synthesized by Pd-catalyzed C–N coupling reaction of 1-bromo-4-(phenylsulfonyl)benzene with 9,9-dimethyl-9,10-dihydroacridine or 9,9′(10*H*,10′*H*)-spirobiacridines. After purification by vacuum sublimation, the chemical structures of the target compounds were characterized by ^{1}H NMR, ^{13}C NMR and high resolution mass spectrometry (HRMS). Their molecular structures were further identified by single crystal X-ray crystallographic analysis. As shown in Fig. 2, **DMAC-1DPS** and **SBA-2DPS** exhibited a twisted configuration with large dihedral angles between the electron donor and acceptor units of 83.8° for **DMAC-1DPS**, and 77.3° and 78.0° for **SBA-2DPS**. Different from the predicted quasi-plane structures of both molecules in DFT simulations, their donor units preferred crooked configurations in the single crystal, which releases the steric hindrance between acridine units and DPS units. Moreover, **SBA-2DPS** possessed a much longer molecular length than **DMAC-1DPS** in the crystal structure, which is in accordance with the DFT results. According to the packing diagram shown in Fig. 2c and d, no obvious π–π stacking contact was observed for both molecules and **SBA-2DPS** aligned orderly parallel to its long axis.

Thermal and electrochemical properties

To evaluate the thermal properties of **DMAC-1DPS** and **SBA-2DPS**, thermogravimetric analysis (TGA) and differential scanning calorimetry (DSC) were performed, and the key data are summarized in Table S1 (ESI†). As depicted in Fig. 3, **SBA-2DPS** exhibited high thermal stability with a decomposition temperature (T_d, with 5% weight loss) of 476 °C, whereas **DMAC-1DPS** showed a much lower T_d of 295 °C. From the DSC curves, the glass transition temperatures (T_gs) of both compounds were determined to be 69 °C and 176 °C for **DMAC-1DPS** and **SBA-2DPS**, respectively. In comparison to the prototypical molecule **DMAC-1DPS**, the improved thermal stability of **SBA-2DPS** is attributed to its more rigid structure and larger molecular weight.[35]

As shown in the cyclic voltammetry curves of both compounds (Fig. S1a, ESI†), **DMAC-1DPS** showed a one-electron oxidation process arising from the DMAC unit, whereas **SBA-2DPS** displayed

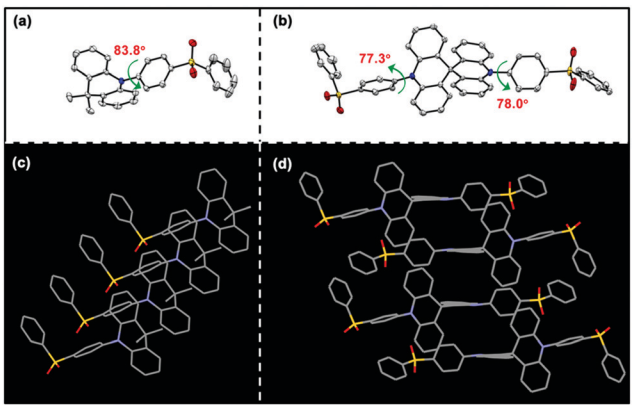

Fig. 2 Oak ridge thermal ellipsoid plot (ORTEP) diagrams of (a) **DMAC-1DPS** and (b) **SBA-2DPS**; (c) molecular packing diagram of **DMAC-1DPS** and (d) molecular parking diagram of **SBA-2DPS** without showing hydrogen atoms and solvent molecules (solvent molecules: chloroform).

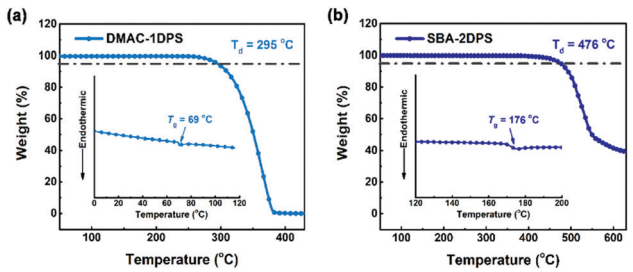

Fig. 3 TGA traces of (a) **DMAC-1DPS** and (b) **SBA-2DPS** recorded at a heating rate of 10 °C min^{-1}. Inset: DSC curves recorded at a heating rate of 10 °C min^{-1}.

a double-electron oxidation process, which may be related to the asymmetrically spatial configuration of its donor SBA moiety.[36] From the onset voltages of the oxidation curves, the HOMO levels were determined to be −5.40 eV for **DMAC-1DPS** and −5.49 eV for **SBA-2DPS**. The deeper HOMO level of **SBA-2DPS** may be ascribed to the weaker electron-donating ability of the SBA moiety. To verify this conjecture, the cyclic voltammograms of SBA and DMAC moieties were obtained. As shown in Fig. S1b (ESI†), the HOMO levels were estimated to be −5.25 eV for SBA and −5.18 eV for DMAC moieties, which coincide well with our expectation. From the estimated energy gaps (E_gs) and HOMO levels of both compounds, their LUMO levels were estimated to be −2.34 eV for **DMAC-1DPS** and −2.42 eV for **SBA-2DPS**. This trend coincides well with the DFT results.

Photophysical properties

As shown in Fig. 4a, a broad and weak absorption around 365 nm was observed for both emitters in toluene solution, which could be assigned to the charge transfer (CT) type transition from the acridine units to the DPS unit. Besides, **DMAC-1DPS** and **SBA-2DPS** showed distinct absorption signals in the shorter wavelength region, which may originate from the local transition of the DPS units and the donor units. With respect to photoluminescence (PL), **DMAC-1DPS** and **SBA-2DPS** showed pure blue emission in toluene with main peaks at 452 nm and 442 nm (Fig. 4a and Table 2), respectively. Their photophysical properties in doped films were also studied by doping these emitters into a widely used host material of bis(2-(diphenylphosphino)phenyl)ether oxide (DPEPO).[37] In comparison with their PL spectra in toluene, the emission peaks of **DMAC-1DPS** and **SBA-2DPS** in doped films slightly bathochromically shifted to 468 nm and 459 nm (Table 2), respectively. Notably, the emission spectra of **SBA-2DPS** is hypsochromic compared with those of **DMAC-1DPS**, no matter in toluene or in the DPEPO host, which may be due to the weaker electron-donating ability of the SBA moiety (as confirmed by CV) and thus weaker intramolecular charge transfer (ICT) transition between the DPS and SBA units.[38] According to the onset wavelengths of fluorescence and phosphorescence spectra (Fig. 4b), the S_1/T_1 values of both emitters were estimated to be 3.04/2.95 eV for **SBA-2DPS**, and 2.98/2.91 eV for **DMAC-1DPS** (Table 2). Correspondingly, ΔE_{ST}s was determined to be 0.09 eV for **SBA-2DPS** and 0.07 eV for **DMAC-1DPS**. Such small values were favourable for boosting the RISC process from T_1 to S_1 with thermal aid. Indeed, the RISC process of both emitters was confirmed by their transient PL decay curves in the doped films as depicted in Fig. 4c. Obviously, their fluorescence intensity showed second-order exponential decays with a delayed ratio over 50% and the lifetimes of the prompt and delayed components were fitted to be 19.0 ns/4.3 μs for **SBA-2DPS** and 20.4 ns/4.2 μs for **DMAC-1DPS** (Table 2). Moreover, the PLQYs of **SBA-2DPS** and **DMAC-1DPS** in the DPEPO host (30 wt%) were measured to be 60% and 61% under argon conditions, suggesting that the emission capability of double D–A emitters is rarely affected. To gain a deeper understanding on their emission properties, related photophysical rate constants

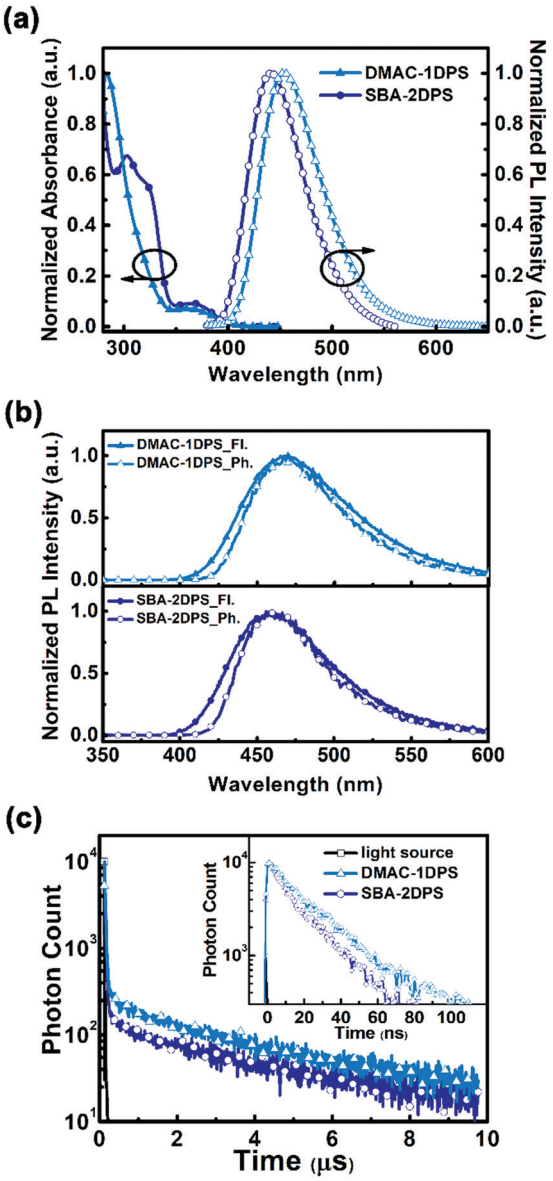

Fig. 4 (a) Normalized UV-vis absorption spectra and PL spectra measured in toluene solutions (1×10^{-5} M) at room temperature. (b) Normalized fluorescence (300 K) and phosphorescence (77 K) spectra of **DMAC-1DPS** and **SBA-2DPS** in DPEPO films with 30 wt% concentration. (c) Transient PL spectra of **DMAC-1DPS** and **SBA-2DPS** in DPEPO films with 30 wt% concentration at room temperature.

were further calculated according to previous reports by assuming that most of the triplet states can return to singlet states through RISC and major nonradiative losses occur in singlet states.[18] As summarized in Table S2 (ESI†), the radiative decay rate from the S_1 state ($k_{r,S}$) of **SBA-2DPS** was estimated to be 1.37×10^7 s^{-1}, which is comparable with the values of conventional fluorescent materials. Meanwhile, its nonradiative decay rate from the S_1 state ($k_{nr,S}$) was determined to be 9.11×10^6 s^{-1}. As for **DMAC-1DPS**, $k_{r,S}$ and $k_{nr,S}$ were estimated to be 0.97×10^7 s^{-1} and 6.17×10^6 s^{-1}, respectively. Although there is a slight difference in $k_{r,S}$ for **DMAC-1DPS** and **SBA-2DPS**, the ratios of $k_{r,S}$ to $k_{nr,S}$ for both emitters are similar (1.50 for **SBA-2DPS** and 1.56 for **DMAC-1DPS**),

Table 2 The summary of the photophysical properties of **DMAC-1DPS** and **SBA-2DPS**

Compound	λ_{abs}[a] [nm]	λ_{em}[a] [nm]	λ_{em}[b] [nm]	τ_p[c] [ns]	τ_d[c] [μs]	Φ_{PL}[d] [%]	Φ_{PF}[d] [%]	Φ_{DF}[d] [%]	S_1/T_1[e] [eV]	ΔE_{ST}[f] [eV]	$\Theta_{\parallel}$[g] [%]
DMAC-1DPS	283	452	468	20.4	4.2	61	20	41	2.98/2.91	0.07	59
SBA-2DPS	303/367	442	459	19.0	4.3	60	26	34	3.04/2.95	0.09	87

[a] Measured in toluene (1×10^{-5} M) at room temperature. [b] Measured in doped DPEPO films (with 30 wt% doping concentration). [c] Lifetime of the prompt and delayed component in transient PL measured in doped DPEPO films (with 30 wt% doping concentration). [d] Photoluminescence quantum yield, the quantum yield of the prompt fluorescence and delayed fluorescence measured in doped DPEPO films (with 30 wt% doping concentration) at room temperature. [e] Obtained from the onset of the fluorescence spectra and phosphorescence spectra doped DPEPO films of these emitters. [f] Calculated from S_1 and T_1. [g] Horizontal dipole ratio measured in doped DPEPO films (with 30 wt% doping concentration) at room temperature.

leading to similar PLQY values. Moreover, **DMAC-1DPS** and **SBA-2DPS** exhibited an effective RISC process with the corresponding rates (k_{RISC}s) of 7.37×10^5 s^{-1} and 5.38×10^5 s^{-1}, respectively, consistent with their small ΔE_{ST}.[39]

In order to study their emitting dipole orientations, the angle- and polarization-resolved PL spectra of **SBA-2DPS** and **DMAC-1DPS** (30 wt% doped in the DPEPO host) were characterized. The *p*-polarized PL intensities *versus* emission angles for both emitters measured at the PL peak wavelength are shown in Fig. 5a and c. In comparison with the simulated curves with different horizontal dipole ratios $\Theta_{\parallel}$($\Theta_{\parallel}$ = 100% represents the fully horizontal dipole orientation and $\Theta_{\parallel}$ = 67% represents the isotropic dipole orientation), the $\Theta_{\parallel}$ of both emitters were extracted as 87% and 59% for **SBA-2DPS** and **DMAC-1DPS**, respectively. These results clearly established that the **SBA-2DPS** exhibited a preferentially horizontal emitting dipole orientation in the DPEPO host; in contrast, the emitting dipole of **DMAC-1DPS** tended to orient more randomly (slightly vertically) in the DPEPO host. To gain deeper insight into the relationship between their $\Theta_{\parallel}$ and molecular structure, TDMs of **SBA-2DPS** and **DMAC-1DPS** were simulated with the nuclear ensemble approach based on the optimized S_1 state geometries (Fig. 5b and d).[40] Although the TDM vectors mainly aligned in the D–A direction for both emitters, smaller components in the *y*–*z* plane were observed for **SBA-2DPS**, suggesting that the TDM orientation of **SBA-2DPS** is more aligned to the molecular axis. As **SBA-2DPS** tends to lie upon the substrate in parallel with the longest axis due to its rod-like shape, the TDMs achieve a preferentially horizontal orientation. Therefore, it is reasonable to attribute the high $\Theta_{\parallel}$ of **SBA-2DPS** to the synergetic result of elongating molecular shape and tuning TDM direction. Besides, the high T_g (176 °C) of **SBA-2DPS** may also contribute to its high $\Theta_{\parallel}$ by decreasing the surface mobility and orientational rearrangement during the vacuum deposition.[41–43] The $\Theta_{\parallel}$ of **SBA-2DPS** in the DPEPO host as a function of doping concentration is also shown in Fig. S2 (ESI†). With the doping concentration varying from 12 wt% to 50 wt%, the $\Theta_{\parallel}$ only showed a slight change from 86% to 89%. This suggests that the horizontal emitting dipole orientation is the intrinsic characteristic of **SBA-2DPS**. Overall, high $\Theta_{\parallel}$ was achieved for the blue emitter **SBA-2DPS** and could be useful in promoting the optical out-coupling efficiency in OLEDs.

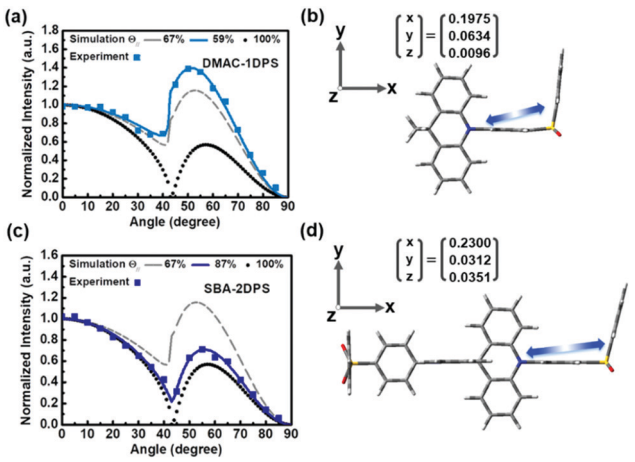

Fig. 5 Measured (symbols) *p*-polarized PL intensity (at PL peak wavelength) *versus* emission angle curves for emitting layers (a) DPEPO: 30 wt% **DMAC-1DPS** (c) DPEPO: 30 wt% **SBA-2DPS**, and simulated curves for the fully horizontal dipole orientation ($\Theta_{\parallel}$ = 100%) and the isotropic dipole orientation ($\Theta_{\parallel}$ = 67%). The direction of the calculated S_0–S_1 transition dipole moment (as indicated by the arrow) of (b) **DMAC-1DPS** and (d) **SBA-2DPS** relative to the coordinates of the molecular structure.

Electroluminescence properties

To evaluate the performance of **SBA-2DPS** upon electrical excitation, we fabricated multilayer OLEDs with structures consisting of indium tin oxide (ITO)/MoO_3 (1 nm)/di-[4-(*N*,*N*-ditolyl-amino)-phenyl]-cyclohexane (TAPC) (40 nm)/*N*,*N*-dicarbazolyl-3,5-benzene (mCP) (10 nm)/bis(2-(diphenylphosphino)phenyl)-ether oxide (DPEPO): 30 wt% **SBA-2DPS** (20 nm)/tris-[3-(3-pyridyl)mesityl]borane (3TPYMB) (50 nm)/LiF (1 nm)/Al, as shown in Fig. 6a. ITO and Al served as the anode and the cathode, respectively. MoO_3 and LiF were used as hole and electron-injection layers, respectively. TAPC and mCP served as hole-transporting layers (HTLs). DPEPO was employed as the host owing to its high energy level of T_1.[37] 3TPYMB was the electron-transporting layer (ETL). For comparison, the reference device with an identical structure but **DMAC-1DPS** as a TADF dopant was also fabricated and tested.

The representative EL characteristics of **SBA-2DPS**- and **DMAC-1DPS**-based devices are shown in Fig. 6c–e, and the key EL data are summarized in Table 3. As shown in Fig. 6c, the EL spectra of **SBA-2DPS** and **DMAC-1DPS** were similar to their PL spectra, with their emission peaks slightly red-shifting to 467 nm and 477 nm, respectively, corresponding to favorable Commission International de l'Eclairage coordinates of (0.15, 0.20) for **SBA-2DPS** and (0.16, 0.26) for **DMAC-1DPS**. Only the emission originating

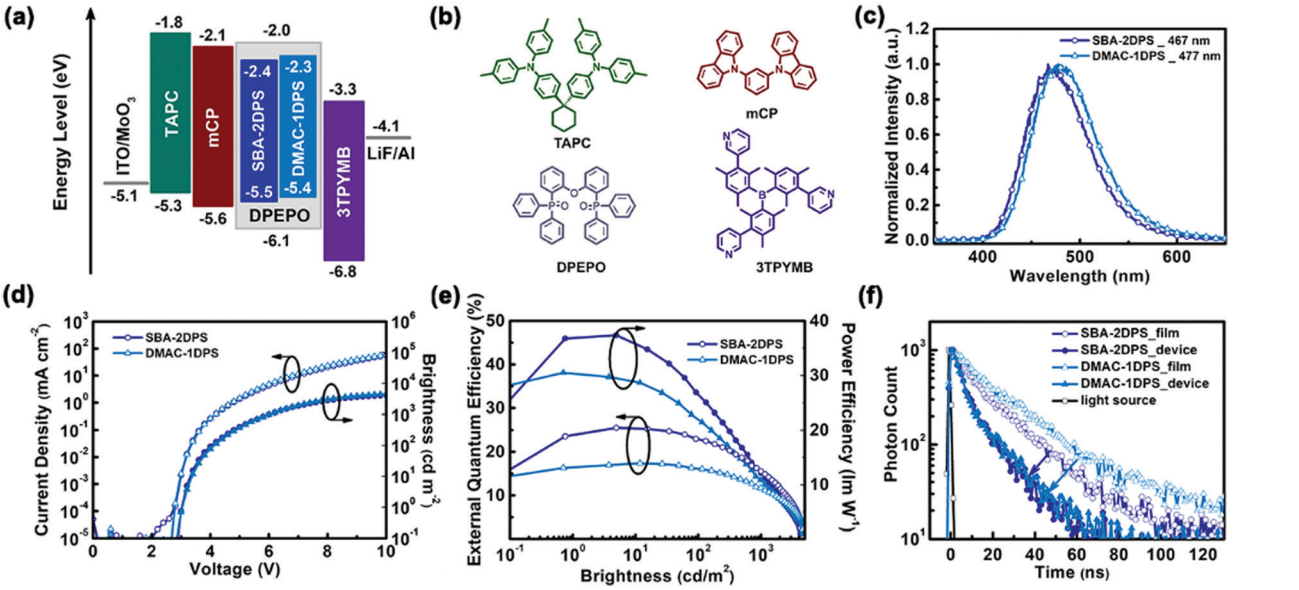

Fig. 6 (a) The energy level diagrams of the devices. (b) Chemical structures of the materials used. (c–e) Electroluminescence spectra, current–voltage–luminance characteristics, external quantum efficiency and power efficiency *versus* luminance curves of devices based on **SBA-2DPS** and **DMAC-1DPS**. (f) The transient PL decay curves of **SBA-2DPS** and **DMAC-1DPS** measured in the single-layer doped films and the complete devices.

from **SBA-2DPS** or **DMAC-1DPS** was observed in the EL spectra, indicating the efficient energy transfer from the host to the TADF dopants. The turn-on voltages of both devices were as low as 2.8 V. **DMAC-1DPS**-based devices achieved a maximum current efficiency (η_c) of 31.0 cd A^{-1}, a maximum power efficiency (η_p) of 30.5 lm W^{-1} and a maximum η_{ext} of 17.4% as shown in Fig. 6d and e. In comparison, devices based on **SBA-2DPS** showed a much superior performance with a maximum η_c of 38.1 cd A^{-1}, a maximum η_p of 37.4 lm W^{-1} and a maximum η_{ext} of 25.5%. To the best of our knowledge, the high η_{ext} of **SBA-2DPS** is superior to most reported TADF devices with coordinate y values ≤ 0.2.[28,29,44] Considering that the TADF characteristics and PLQY of SBA-DPS are similar to those of **DMAC-1DPS**, the superior performance of SBA-DPS-based devices could be attributed to their higher horizontal dipole ratio ($\Theta_{\parallel}$ = 87%), which will boost the optical out-coupling efficiency (Φ_{out}) of the devices. Indeed, the Φ_{out} values were estimated to be 38.2% and 24.7% for SBA-DPS and **DMAC-1DPS**-based devices (Table 3) by using the classical oscillating dipole model and $\Theta_{\parallel}$, which indicates the great importance of the horizontal dipole orientation in improving Φ_{out}. In this case, the upper limit of η_{ext}s can be calculated by $\eta_{ext} = \Phi_{PL} \times \Phi_{out}$ by assuming perfect carrier balance and unit exciton utilization in eqn (1). Unexpectedly, the theoretically predicted upper limits of η_{ext} (22.9% for **SBA-2DPS** devices and 15.1% for **DMAC-1DPS** devices, Table 3) were slightly lower than their actual experimental maximum η_{ext}s, indicating that additional mechanisms may contribute to the obtained device performance. Some previous studies have revealed that the effective emission quantum yield (q_{eff}) of an emitter in the device configuration may exceed the measured Φ_{PL}, owing to the modification of the spontaneous radiative transition rate by the dipole-field interaction induced by the optical microcavity effect.[45–47] To verify the influence of optical microcavities on our system, the transient PL decay curves of **SBA-2DPS** and **DMAC-1DPS** in the completed device configurations were obtained. As shown in Fig. 6f, the prompt decay lifetimes significantly decreased from 19.0 ns (in the thin film) to 13.0 ns (in the device configuration) for **SBA-2DPS** and 20.4 ns to 12.1 ns for **DMAC-1DPS**. These results confirm the non-negligible effect of optical microcavity on enhancing the quantum yield of these emitters. To further estimate q_{eff} in the device, the Purcell factor (F), defined as the modification ratio of the emitter radiative transition rate in the device to that in the thin-film configuration, was simulated to be 1.48 for **SBA-2DPS** and 1.71 for **DMAC-1DPS** (Table 3).[48–50] According to previous studies,[20,46] q_{eff} values were then calculated to be 68.9% for **SBA-2DPS** and 72.8% for **DMAC-1DPS**, which surpass their thin-film Φ_{PL} values measured on the fused silica substrate. Correspondingly, the upper limit η_{ext} values were recalculated with the

Table 3 The key electroluminescence data

Device	V_{on}[a] [V]	EL_{peak} [nm]	η_c[b] [cd A^{-1}]	η_p[b] [lm W^{-1}]	η_{ext}[b] [%]	Φ_{out}[c] [%]	Φ_{PL} Φ_{out} [%]	F[d]	q_{eff}[e] [%]	q_{eff} Φ_{out} [%]	CIE (x,y)
SBA-2DPS	2.8	467	38.1, 34.1, 23.5	37.4, 26.4, 12.3	25.5, 22.9, 15.6	38.2	22.9	1.48	68.9	26.3	0.15, 0.20
DMAC-1DPS	2.8	477	31.0, 29.0, 20.9	30.5, 21.8, 10.9	17.4, 16.2, 11.6	24.7	15.1	1.71	72.8	18.0	0.16, 0.26

[a] The turn-on voltage recorded at a brightness of 0.1 cd m^{-2}. [b] The maximum value, values at 100 and 1000 cd m^{-2}. [c] The calculated optical out-coupling efficiency. [d] The calculated Purcell factor in the device configuration relative to that in thin films. [e] The calculated effective radiative quantum efficiency in the device configuration.

effective emission quantum yield ($q_{eff} \times \Phi_{out}$ = 26.3% for **SBA-2DPS**-based devices and 18.0% for **DMAC-1DPS**-based devices), which were slightly higher than the experimental values. Thus, it is reasonable to regard the optical microcavity effect as another underlying mechanism that contributes to the high EL performance of **SBA-2DPS**-based devices, in addition to the preferentially horizontal emitting dipole orientation. Nevertheless, a much superior EL performance was achieved for molecule **SBA-2DPS** compared to its prototypical molecule **DMAC-1DPS**. This demonstrates the validity of the spiro-linked double D–A molecular architecture on constructing excellent TADF emitters with a preferentially horizontal emitting dipole orientation for highly efficient blue OLEDs.

Conclusions

In summary, a spiro-linked double D–A molecular architecture has been introduced to construct blue TADF emitters with a preferentially horizontal emitting dipole orientation. Using this strategy, a rod-liked TADF emitter, namely **SBA-2DPS**, has been designed and synthesized. Compared with the prototypical molecule **DMAC-1DPS**, **SBA-2DPS** exhibited a much elongated configuration while maintaining relatively high S_1/T_1 energy levels owing to the σ-spacer linkage. Favourably, **SBA-2DPS** exhibited higher thermal stability, maintained the PLQY and showed a distinct TADF feature. Most importantly, **SBA-2DPS** also showed a preferentially horizontal emitting dipole orientation with a high $\Theta_{\parallel}$ of 87%. Compared with **DMAC-1DPS**-based devices, blue OLEDs employing **SBA-2DPS** as the emitter exhibited a significantly higher η_{ext} value of 25.5% with CIE coordinates of (0.15, 0.20) in pure blue, suggesting the great contribution of the horizontal emitting dipole orientation to enhancing the OLED performance. Further analysis has revealed that the optical microcavity effect also played an important role in boosting the internal quantum efficiency of **SBA-2DPS** in devices and thus the device performance. Overall, this work demonstrated the great potential of spiro-linked double D–A emitters in achieving highly efficient blue OLEDs. Further work on developing deep-blue TADF emitters with a higher $\Theta_{\parallel}$ and a higher PLQY using this strategy is in progress.

Experimental section

All reagents were used as received from commercial sources and used as received unless otherwise stated. 1-Bromo-4-(phenylsulfonyl)benzene[51] and 9,9′(10*H*,10′*H*)-spirobiacridines (SBA)[52] were synthesized according to the previous literature.

Synthesis of 9,9-dimethyl-10-(4-(phenylsulfonyl)phenyl)-9,10-dihydroacridine (DMAC-1DPS)

1-Bromo-4-(phenylsulfonyl)benzene (977 mg, 3.3 mmol), 9,9-dimethyl-9,10-dihydroacridine (627 mg, 3.0 mmol), sodium *tert*-butoxide (317 mg, 3.3 mmol), palladium(II) acetate (20 mg, 0.09 mmol) and tri-*tert*-butylphosphine tetrafluoroborate (78 mg, 0.27 mmol) were dissolved in dry toluene (15 mL) under an argon atmosphere. After stirring at 110 °C for 24 hours, the suspension was cooled to 298 K, mixed thoroughly with dichloromethane and washed with water three times. After drying with anhydrous Na_2SO_4, the organic phase was concentrated and the crude product was purified by column chromatography on silica gel with petroleum ether/dichloromethane (2 : 1 by vol.) as the eluent. Finally, the product was obtained as a white powder (1.16 g, yield: 91%). ^{1}H NMR (400 MHz, $CDCl_3$ + TMS, 298 K) δ (ppm): 8.17 (d, J = 8 Hz, 2H), 8.07 (d, J = 8 Hz, 2H), 7.68–7.58 (m, 3H), 7.51–7.46 (m, 4H), 7.00–6.95 (m, 4H), 6.27–6.23 (m, 2H), 1.66 (s, 6H). ^{13}C NMR (100 MHz, $CDCl_3$, 298 K) δ (ppm): 146.4, 141.3 140.6, 140.2, 133.5, 131.4, 131.0, 130.4, 129.5, 127.9, 126.4, 125.4, 121.6, 114.8, 36.2, 30.9. HRMS (electrospray ionization (ESI)): m/z $[M + H]^+$ calcd for $C_{27}H_{24}NO_2S^+$: 426.1522; found: 426.1522.

Synthesis of 10,10′-bis(4-(phenylsulfonyl)phenyl)-10*H*,10′*H*-9,9′-spirobiacridine (SBA-2DPS)

SBA-2DPS was prepared according to a similar procedure to **DMAC-1DPS**. Yield: 87%. ^{1}H NMR (400 MHz, $CDCl_3$ + TMS, 298 K) δ (ppm): 8.28 (d, J = 8 Hz, 4H), 8.10 (d, J = 8 Hz, 4H), 7.69–7.60 (m, 10H), 7.09 (d, J = 8 Hz, 4H), 6.87 (t, J = 8 Hz, 4H), 6.75 (t, J = 8 Hz, 4H), 6.14 (d, J = 8 Hz, 4H). ^{13}C NMR (100 MHz, $CDCl_3$, 298 K) δ (ppm): 146.0, 141.8, 141.0, 137.7, 133.7, 132.8, 132.8, 131.7, 130.7, 129.6, 128.1, 126.8, 121.5, 113.8, 46.7. HRMS (ESI): m/z $[M + H]^+$ calcd for $C_{49}H_{35}N_2O_4S_2^+$: 779.2033; found: 779.2013.

Author contributions

X. Zeng, S. Gong, C.-C. Wu and C. Yang wrote the manuscript. X. Zeng, X. Xiao and L. Zhan synthesized the compounds. X. Zeng measured the photophysical, thermal and electrochemical properties of the compounds. K.-C. Pan, W.-K. Lee and C.-C. Wu fabricated and characterized the devices. F. Ni, S. Gong and C. Yang conceived the original idea for investigation. Y. Xiang and Y. Zhang performed the X-ray single crystal diffraction analysis. W. Zeng performed the quantum chemical calculations. All authors discussed the progress of research and reviewed the manuscript.

Conflicts of interest

There are no conflicts to declare.

Acknowledgements

The authors gratefully acknowledge financial support from the National Key R&D Program of China (2016YFB0401002), the National Natural Science Foundation of China (51873158, 51573141, 91833304 and 91433201), the National Basic Research Program of China (973 Program 2015CB655002), the Shenzhen Peacock Plan (KQTD20170330110107046), the Key Technological Innovation Program of Hubei Province (2018AAA013), and the Natural Science Foundation for Distinguished Young Scholars of Hubei Province (2017CFA033). C. C. Wu acknowledges the support from the Ministry of Science and

Technology of Taiwan (MOST 105-2221-E-002-162-MY3 and 107-2221-E-002-160-MY3). The numerical calculations in this paper have been done using the supercomputing system at the Supercomputing Center of Wuhan University.

Notes and references

1 M. C. Gather, A. Köhnen and K. Meerholz, *Adv. Mater.*, 2011, **23**, 233–248.
2 T. Sekitani and T. Someya, *Adv. Mater.*, 2010, **22**, 2228–2246.
3 C. W. Tang and S. A. VanSlyke, *Appl. Phys. Lett.*, 1987, **51**, 913–915.
4 M. A. Baldo, D. F. O'Brien, Y. You, A. Shoustikov, S. Sibley, M. E. Thompson and S. R. Forrest, *Nature*, 1998, **395**, 151–154.
5 J. Partee, E. L. Frankevich, B. Uhlhorn, J. Shinar, Y. Ding and T. J. Barton, *Phys. Rev. Lett.*, 1999, **82**, 3673–3676.
6 H. Uoyama, K. Goushi, K. Shizu, H. Nomura and C. Adachi, *Nature*, 2012, **492**, 234–238.
7 Y. Xu, X. Liang, X. Zhou, P. Yuan, J. Zhou, C. Wang, B. Li, D. Hu, X. Qiao, X. Jiang, L. Liu, S.-J. Su, D. Ma and Y. Ma, *Adv. Mater.*, 2019, **31**, 1807388.
8 T. Tsutsui, E. Aminaka, C. P. Lin and D.-U. Kim, *Philos. Trans. R. Soc., A*, 1997, **355**, 801–814.
9 K. Meerholz and D. C. Müller, *Adv. Funct. Mater.*, 2001, **11**, 251–253.
10 M. A. Baldo, D. F. O'Brien, M. E. Thompson and S. R. Forrest, *Phys. Rev. B: Condens. Matter Mater. Phys.*, 1999, **60**, 14422–14428.
11 Y. Tao, K. Yuan, T. Chen, P. Xu, H. Li, R. Chen, C. Zheng, L. Zhang and W. Huang, *Adv. Mater.*, 2014, **26**, 7931–7958.
12 N. A. Kukhta, T. Matulaitis, D. Volyniuk, K. Ivaniuk, P. Turyk, P. Stakhira, J. V. Grazulevicius and A. P. Monkman, *J. Phys. Chem. Lett.*, 2017, **8**, 6199–6205.
13 A. Tsuboyama, H. Iwawaki, M. Furugori, T. Mukaide, J. Kamatani, S. Igawa, T. Moriyama, S. Miura, T. Takiguchi, S. Okada, M. Hoshino and K. Ueno, *J. Am. Chem. Soc.*, 2003, **125**, 12971–12979.
14 Q. Zhang, B. Li, S. Huang, H. Nomura, H. Tanaka and C. Adachi, *Nat. Photonics*, 2014, **8**, 326–332.
15 Y. Tao, C. Yang and J. Qin, *Chem. Soc. Rev.*, 2011, **40**, 2943–2970.
16 L. Xiao, Z. Chen, B. Qu, J. Luo, S. Kong, Q. Gong and J. Kido, *Adv. Mater.*, 2011, **23**, 926–952.
17 W.-Y. Wong and C.-L. Ho, *J. Mater. Chem.*, 2009, **19**, 4457–4482.
18 K.-C. Pan, S.-W. Li, Y.-Y. Ho, Y.-J. Shiu, W.-L. Tsai, M. Jiao, W.-K. Lee, C.-C. Wu, C.-L. Chung, T. Chatterjee, Y.-S. Li, K.-T. Wong, H.-C. Hu, C.-C. Chen and M.-T. Lee, *Adv. Funct. Mater.*, 2016, **26**, 7560–7571.
19 K. Wu, T. Zhang, Z. Wang, L. Wang, L. Zhan, S. Gong, C. Zhong, Z.-H. Lu, S. Zhang and C. Yang, *J. Am. Chem. Soc.*, 2018, **140**, 8877–8886.
20 W. Zeng, H.-Y. Lai, W.-K. Lee, M. Jiao, Y.-J. Shiu, C. Zhong, S. Gong, T. Zhou, G. Xie, M. Sarma, K.-T. Wong, C.-C. Wu and C. Yang, *Adv. Mater.*, 2018, **30**, 1704961.
21 S.-Y. Kim, W.-I. Jeong, C. Mayr, Y.-S. Park, K.-H. Kim, J.-H. Lee, C.-K. Moon, W. Brütting and J.-J. Kim, *Adv. Funct. Mater.*, 2013, **23**, 3896–3900.
22 D. H. Ahn, S. W. Kim, H. Lee, I. J. Ko, D. Karthik, J. Y. Lee and J. H. Kwon, *Nat. Photonics*, 2019, **13**, 540–546.
23 T.-A. Lin, T. Chatterjee, W.-L. Tsai, W.-K. Lee, M.-J. Wu, M. Jiao, K.-C. Pan, C.-L. Yi, C.-L. Chung, K.-T. Wong and C.-C. Wu, *Adv. Mater.*, 2016, **28**, 6976–6983.
24 C. Mayr, S. Y. Lee, T. D. Schmidt, T. Yasuda, C. Adachi and W. Brütting, *Adv. Funct. Mater.*, 2014, **24**, 5232–5239.
25 K.-H. Kim and J.-J. Kim, *Adv. Mater.*, 2018, **30**, 1705600.
26 D. Yokoyama, *J. Mater. Chem.*, 2011, **21**, 19187–19202.
27 M. Liu, R. Komatsu, X. Cai, K. Hotta, S. Sato, K. Liu, D. Chen, Y. Kato, H. Sasabe, S. Ohisa, Y. Suzuri, D. Yokoyama, S.-J. Su and J. Kido, *Chem. Mater.*, 2017, **29**, 8630–8636.
28 T.-T. Bui, F. Goubard, M. Ibrahim-Ouali, D. Gigmes and F. Dumur, *Appl. Sci.*, 2018, **8**, 494.
29 M. Y. Wong and E. Zysman-Colman, *Adv. Mater.*, 2017, **29**, 1605444.
30 F. B. Dias, T. J. Penfold and A. P. Monkman, *Methods Appl. Fluoresc.*, 2017, **5**, 012001.
31 A. Pershin, D. Hall, V. Lemaur, J.-C. Sancho-Garcia, L. Muccioli, E. Zysman-Colman, D. Beljonne and Y. Olivier, *Nat. Commun.*, 2019, **10**, 597.
32 M. K. Etherington, J. Gibson, H. F. Higginbotham, T. J. Penfold and A. P. Monkman, *Nat. Commun.*, 2016, **7**, 13680.
33 T. Lu and F. Chen, *J. Mol. Graphics Modell.*, 2012, **38**, 314–323.
34 C. S. Oh, C.-K. Moon, J. M. Choi, J.-S. Huh, J.-J. Kim and J. Y. Lee, *Org. Electron.*, 2017, **42**, 337–342.
35 C. Fan, Y. Chen, Z. Liu, Z. Jiang, C. Zhong, D. Ma, J. Qin and C. Yang, *J. Mater. Chem. C*, 2013, **1**, 463–469.
36 P. L. dos Santos, J. S. Ward, D. G. Congrave, A. S. Batsanov, J. Eng, J. E. Stacey, T. J. Penfold, A. P. Monkman and M. R. Bryce, *Adv. Sci.*, 2018, **5**, 1700989.
37 C. Han, Y. Zhao, H. Xu, J. Chen, Z. Deng, D. Ma, Q. Li and P. Yan, *Chem. – Eur. J.*, 2011, **17**, 5800–5803.
38 I. S. Park, S. Y. Lee, C. Adachi and T. Yasuda, *Adv. Funct. Mater.*, 2016, **26**, 1813–1821.
39 X. Cai, X. Li, G. Xie, Z. He, K. Gao, K. Liu, D. Chen, Y. Cao and S.-J. Su, *Chem. Sci.*, 2016, **7**, 4264–4275.
40 W. Zeng, S. Gong, C. Zhong and C. Yang, *J. Phys. Chem. C*, 2019, **123**, 10081–10086.
41 S. S. Dalal and M. D. Ediger, *J. Phys. Chem. Lett.*, 2012, **3**, 1229–1233.
42 C. Mayr and W. Brütting, *Chem. Mater.*, 2015, **27**, 2759–2762.
43 D. Yokoyama, A. Sakaguchi, M. Suzuki and C. Adachi, *Appl. Phys. Lett.*, 2008, **93**, 173302.
44 X.-L. Chen, J.-H. Jia, R. Yu, J.-Z. Liao, M.-X. Yang and C.-Z. Lu, *Angew. Chem., Int. Ed.*, 2017, **129**, 15202–15205.
45 A. Dodabalapur, L. J. Rothberg, T. M. Miller and E. W. Kwock, *Appl. Phys. Lett.*, 1994, **64**, 2486–2488.
46 T. D. Schmidt, D. S. Setz, M. Flämmich, J. Frischeisen, D. Michaelis, B. C. Krummacher, N. Danz and W. Brütting, *Appl. Phys. Lett.*, 2011, **99**, 163302.

47 N. Takada, T. Tsutsui and S. Saito, *Appl. Phys. Lett.*, 1993, **63**, 2032–2034.
48 H. Becker, S. E. Burns and R. H. Friend, *Phys. Rev. B: Condens. Matter Mater. Phys.*, 1997, **56**, 1893–1905.
49 X.-W. Chen, W. C. H. Choy, C. J. Liang, P. K. A. Wai and S. He, *Appl. Phys. Lett.*, 2007, **91**, 221112.
50 B. C. Krummacher, S. Nowy, J. Frischeisen, M. Klein and W. Brütting, *Org. Electron.*, 2009, **10**, 478–485.
51 G. Zhou, Q. Wang, X. Wang, C.-L. Ho, W.-Y. Wong, D. Ma, L. Wang and Z. Lin, *J. Mater. Chem.*, 2010, **20**, 7472–7484.
52 M. Ooishi, M. Seino, R. Imachi, T. Ishida and T. Nogami, *Tetrahedron Lett.*, 2002, **43**, 5521–5524.